

# Development of a fragment kinetic Monte Carlo method for efficient prediction of ionic diffusion in perovskite crystals

Hiroya Nakata<sup>1, a)</sup>

*Kyocera Corporation, Research Institute for Advanced Materials and Devices,  
3-5-3 Hikaridai Seika-cho Soraku-gun Kyoto 619-0237, Japan.*

A massively parallel kinetic Monte Carlo (kMC) approach is proposed for simulating ionic migration in a crystal system by introducing the atomic fragmentation scheme (fragment kMC). The fragment kMC method achieved a reasonable parallel efficiency with 1728 central processing unit (CPU) cores, and the method enables the simulation of ionic diffusion in  $\mu\text{m}$ -scale perovskite crystals. To demonstrate the feasibility of the proposed approach, the fragment kMC method was applied to predict the diffusion coefficients of hydride ions and oxygen ions in  $\text{SrTiO}_{(3-x)}\text{H}_x$  and  $\text{BaTiO}_{(3-x)}\text{H}_x$  systems. Finally, the fragment kMC method was customized for  $\mu$ -scale  $\text{BaTiO}_3$  simulation under an applied bias voltage, and oxygen diffusion in  $\text{BaTiO}_3$  model was evaluated. The respective grain sizes are sub-nanometre, and we conclude that the proposed fragment kMC method can be applied to calculate the extent of ionic migration in  $\mu$ -scale materials with fully atomistic simulation models at a reasonable computational cost.

## I. INTRODUCTION

Perovskite material, which is typically composed of an  $\text{ABO}_3$  type stoichiometry with a cubic crystal structure, draws considerable attention, because of its applicability in many electronic devices that are important for industry. The potential application fields include sensors<sup>1,2</sup>, random access memory<sup>3-5</sup>, batteries<sup>6,7</sup>, capacitors<sup>8,9</sup>, piezoelectric devices<sup>10,11</sup>, solid fuel cells<sup>12</sup>, and catalysts for the water-splitting reaction<sup>13</sup>.

In all these applications, the stability and migration of oxygen vacancies are a key factor for determining the utility of the electronic devices. For example, the blocking the oxygen vacancies diffusion by the grain boundaries is one of the important factor for the long-term failure of multilayer ceramic capacitors (MLCCs), and a number of experimental studies of the degradation mechanism have been reported<sup>14-21</sup>. For these reasons, experimental investigations of oxygen diffusion in perovskite oxides played a central role in designing highly functional materials for

<sup>a)</sup>Electronic mail: hiroya.nakata.gt@kyocera.jp

industrial devices<sup>22–28</sup>.

Until recently, ionic migration was empirically predicted according to the ionic radius and size of the unit cell. With the development of computer science, a more detailed analysis of the diffusion mechanisms can be performed for a more sophisticated design towards the development of highly functional materials. Therefore, theoretical simulations are becoming powerful tools for understanding the vacancy-mediated ionic diffusion. In particular, quantum mechanics (QM)-based analysis of vacancy diffusion in perovskite crystal structures has been performed intensively for  $\text{BaTiO}_3$ <sup>29–32</sup>,  $\text{SrTiO}_3$ <sup>33,34</sup>,  $\text{BaZrO}_3$ <sup>35,36</sup>, and many other perovskite crystal structure materials<sup>37–39</sup>. The above QM approaches were mostly limited to static analysis of phenomena such as formation enthalpy and activation barriers because of the high computational cost. To focus on the kinetics of the ionic migration, the stability of vacancies near the grain boundary, crystal dislocation, or crystal transition, a number of molecular dynamics (MD) simulations were performed for the bulk<sup>40–44</sup>, surface or interface<sup>45</sup>, and dislocations<sup>46</sup>. Although the above MD simulations can cover most ionic migration behaviours, the applications are limited within the ionic diffusion of oxygen in the relatively high-temperature region (more than 1000 K), the system size

is within several  $\text{nm}^3$ , and the simulation time scale is several ns. However, for a typical electronic device operating environment, the temperature range is between 300 K and 500 K, and the material sizes are around  $1 \mu\text{m}$ . Thus, it is necessary to develop an alternative approach to simulate the ionic migration in such low-temperature regions with much larger computational models.

The kinetic Monte Carlo (kMC) method<sup>47–49</sup> is one of the promising approaches towards such large-scale ionic migration simulation. kMC enables one to calculate long-time scale simulations, in which the vacancy jumps into a different nearest site based on the predefined transition probability. kMC has been applied to predict the kinetics of many problems, such as yttria-stabilized zirconia<sup>50–52</sup>, oxygen diffusion in doped ceria<sup>53,54</sup>, chemical reactions<sup>55–61</sup>, material diffusion<sup>62–66</sup>, electrochemical impedance<sup>67</sup>, chemical catalysis<sup>68–74</sup>, adsorbate–adsorbate interactions,<sup>75,76</sup> and crystal growth<sup>77,78</sup>. Despite the success of the kMC approach, there are basically two limitations to applying the method to oxygen migration in perovskite crystal structures. First, the simulation time scale decreases with the increase in system size. Second, the efficient parallel programming of ionic migration for kMC is difficult. The update of the event list

and their selection can be straightforwardly estimated at minor computational cost, but the bottleneck is the communication between the boundary regions of the respective parallelized lattice. Thus, despite the mentioned success of the kMC approach, a more sophisticated approach is necessary towards the simulation of ionic migration in  $\mu\text{m}$ -scale ceramic materials.

To reduce the computational cost of kMC approach, several group developed parallel version of kMC based on the block separation, which separate the kMC event selection based on the respective predefined block groups<sup>52,79</sup>. Even these success of the parallel approach, the method require further development to simulate much more complex chemical reaction and ionic diffusions. In this study, we propose a highly efficient approach of ionic migration simulation, in which the kMC simulation is fragmented based on the respective atoms (fragment kMC). Then, the complex event selection and its parallelization can be decomposed into the respective fragments. The fragment kMC approach shows a reasonable parallel efficiency with a large number of central processing unit (CPU) cores. Subsequently, we discuss the effectiveness of the fragment kMC approach by applying the method to predict the diffusion of the hydride ion in the  $\text{SrTiO}_{(3-x)}\text{H}_x$  and  $\text{BaTiO}_{(3-x)}\text{H}_x$  systems. It is experimen-

tally known that diffusion of the hydride ion is vacancy-mediated, and its diffusion coefficient depends significantly on the concentration of hydride ions<sup>80</sup>. We demonstrate that the fragment kMC approach can straightforwardly predict the diffusion coefficients in such complex ionic migrations. Second, the oxygen migration in  $\text{BaTiO}_3$  was evaluated under applied voltage. To make a  $\mu$ -scale model, the computational model contained 7,680,000,000 atoms, and the simulation time was 5 ms. In this study, the effectiveness of fragment kMC was demonstrated by performing vacancy migration for several specific examples related to energy and electronic devices, and we opened up a new territory of application of atomistic material simulation in large-scale diffusion analysis.

## II. THEORETICAL METHOD

### A. Summary of the conventional kMC method

In this section, we briefly summarize the conventional kMC approach, and more details can be found in many places<sup>47-49</sup>. In the jump-diffusion kMC approach, the transition rate for the  $i$ th event,  $k_i$ , is evaluated based on the rate constant of the chemical reaction as follows:

$$k_i = A \exp \left[ -\frac{E_a}{RT} \right], \quad (1)$$

where  $E_a$ ,  $R$ ,  $T$ , and  $A$  are the activation energy, universal gas constant, temperature, and pre-exponential factor, respectively. Then, the transition probability for the  $i$ th event  $p_i$  is estimated by

$$p_i = \frac{k_i}{\sum_j k_j}. \quad (2)$$

Based on the probability  $p_i$ , one of the events is chosen, and the geometry is updated according to the selected event. To select an event, typically, a random number  $r$  is generated, and then one can define the selected event  $l$  so as to satisfy the following equation:

$$\sum_i^l k_i / \sum_i^N k_i \leq r \leq \sum_i^{l+1} k_i / \sum_i^N k_i, \quad (3)$$

where  $N$  is the number of total event. The geometry and the transition probability  $p_i$  for respective events are updated according to the selected event  $l$ , and  $n + 1$ th step simulation time  $t_{n+1}$  is also updated by another random number,  $r'$ , as follows:

$$t_{n+1} = t_n - \frac{\ln(r')}{\sum_i k_i}. \quad (4)$$

Despite its simple theory and algorithm, the application of kMC to a large system is sometimes difficult, because there are basically two bottlenecks for practical application of the kMC simulation. First, it is not difficult to see that the time step shown in Eq. (4) becomes smaller and smaller when the number of events in the system increases. Second, the sequential event selection and event

update are difficult to parallelize. As a result, the application territory of the standard kMC method is limited within a relatively small size of the computational model and a short simulation time in the case of the jump-diffusion approach.

## B. Atomic-based fragment kMC method

Towards the simulation of microscale kinetics of atomic diffusion and its massive parallel algorithm, the rate constant of the chemical reaction in Eq. (1) can be rewritten with atomic-based formulation as follows:

$$k_i^I = A \exp \left[ -\frac{E_a}{RT} \right], \quad (5)$$

where  $I$  is the atomic index. Then, the total rate for each atom  $R_I$  and the maximum rate constant  $R^{\max}$  are

$$R_I = \sum_{i \in I} k_i^I, \quad (6)$$

$$R^{\max} = \max(R_I). \quad (7)$$

Using the maximum rate constant  $R^{\max}$ , the transition probability  $p_i$  is reformulated as

$$p_i = \frac{R^{\max}}{\sum_J \sum_j k_j^J} \frac{k_i}{R^{\max}}, \quad (8)$$

and the probability to select atom  $I$  ( $p^I$ ) is

$$p^I = \sum_{j \in I} p_j^I \quad (9)$$

$$= \frac{R^{\max}}{\sum_J \sum_j k_j^J} \sum_{j \in I} \frac{k_j}{R^{\max}}. \quad (10)$$

The first term in Eq. (10) is independent of fragment  $I$ , which means that the selection probability only depends on the rate constants related to atom  $I$ . This concept of dynamic renormalization can be also found in the study Grieshammer et. al.<sup>81</sup>.

By introducing the auxiliary value  $R^{\max}$ , the event selection can be decomposed into selection of atoms and of events. Then, the kMC algorithm can be reformulated (see Figure 1). First,  $N^{\text{frg}}$  atoms in the system are selected randomly (there are three selected atoms in Figure 1 for example). Then, for each selected atom, the events are chosen based on the transition probability  $\frac{k_i}{R^{\max}}$ . If the total transition rate constant  $\sum_{i \in I} k_i$  is less than  $R^{\max}$ , we introduce a vacancy event region, where no atomic transition and no time integration occur. With the pseudo-event selection, the probability of selecting each event is exactly the same as the original formulation of the transition probability shown in Eq. (2), and each event can be updated independently.

This fragmentation of the event update procedure enables performing an efficient parallel implementation of kMC for atomic diffusion or for a chemical reaction. Then, all the related event lists are gathered, and the rate constant for the next stage of event selection is updated. Simultaneously, the next step simulation time  $t_{n+1}$  is incremented as

$$t_{n+1} = t_n - \frac{\ln(r')}{\sum_i k_i} N^{\text{updated}}, \quad (11)$$

where  $N^{\text{updated}}$  is the event number except that the selected event is null. Thus, if the number of the updated event  $N^{\text{updated}}$  is more than one, the event and corresponding atoms are updated independently.

### III. COMPUTATIONAL DETAILS

The fragment kMC approach was implemented into the kMC programme (written in C++), and the programme was parallelized with message passing interface (MPI). (the fragment kMC programme is available free of charge at GitHub (<https://github.com/hiroyanakata/kMC.v01>)).

As for the pilot test of the developed programme, the vacancy diffusion in SrTiO<sub>3</sub> and BaTiO<sub>3</sub> single perovskite crystals was evaluated (see Figure 2 for the crystal structure). The hydride ions diffusion in SrTiO<sub>3</sub> was recently reported by Liu et al.<sup>80</sup>, but the diffusion coefficient for each hydride and oxygen ion separately is not yet clearly understood. Thus, in this study, the hydride ions diffusion in perovskite SrTiO<sub>(3-x)</sub>H<sub>x</sub> and BaTiO<sub>(3-x)</sub>H<sub>x</sub> was also evaluated, where  $x = 0.25, 0.35, \text{ and } 0.45$ . The activation energies  $E_a$  for the vacancy diffusion of oxygen are 0.6 eV for SrTiO<sub>3</sub><sup>28,82</sup> and 0.7 eV

for BaTiO<sub>3</sub><sup>83</sup>, which were verified by experiment. Because there is no experimental study of the activation barrier of a pure hydride ions, the activation energy of hydride ions was estimated from a previous first principle calculation<sup>80,84</sup>; the activation barrier of hydride ions was chosen as 0.17 and 0.28 eV for SrTiO<sub>3</sub> and BaTiO<sub>3</sub>, respectively. For all the simulation, the pre-exponential factor  $A$  is set to 1.0e13 (1/s).

First, the accuracy of the developed fragment kMC was evaluated by comparing with the standard kMC. Then, the parallel efficiency of fragment kMC was evaluated by performing a million-step kMC simulation, and the computational timing was evaluated from a single core to 1728 cores. The system size was 600<sup>3</sup> unit cells for the performance tests, while we used a relatively large system size (1200<sup>3</sup> unit cells) for evaluation of the parallel efficiency from 32 to 1728 cores; 0.1% of oxygen atoms in the crystal were replaced with vacancies.

Second, the hydride ions and oxygen diffusion coefficients were evaluated for the temperature range from 550 to 700 K. Then, the apparent activation barrier was evaluated by the Arrhenius plot. In this study, the diffusion coefficients for hydride ions and oxygen were separately evaluated by tracking the trajectory of the respective atoms.

Finally, to demonstrate the effectiveness

of the fragment kMC approach, the oxygen vacancy diffusion in  $\mu$  scale BaTiO<sub>3</sub> was evaluated under an applied voltage. To consider the effect of the applied voltage, the electrostatic potential was considered by solving the Poisson equation, and the effect of electrostatic potential (ESP) on the rate constant was included as follows:

$$k_i^I = A \exp \left[ -\frac{E_a + \Delta E_{\text{pot}}}{RT} \right], \quad (12)$$

where  $\Delta E_{\text{pot}}$  is the ESP difference between product and reactant position. The system size was 641.6 nm  $\times$  160.4 nm  $\times$  962.4 nm, which is nearly the experimental size of a ferroelectric material, and the total number of atoms was 7,680,000,000. To run such a large-scale computational model, the simulation was performed with 1536 CPU cores. The detailed calculation model is shown in the next section.

## IV. RESULTS AND DISCUSSION

### A. Accuracy and parallel efficiency of the fragment kMC method

To investigate the accuracy of the fragment kMC approach, the simulation results of vacancy diffusion were compared between different numbers of fragments from  $N^{\text{frg}} = 1$  (conventional kMC) to  $N^{\text{frg}} = 216$ , and the parallel efficiencies of the respective fragment patterns were evaluated to demonstrate the

effectiveness of the developed approach. For this purpose, the vacancy diffusion coefficients in  $\text{SrTiO}_3$  and  $\text{SrTiO}_{2.75}\text{H}_{0.25}$  were investigated.

The simulation results for various numbers of fragments  $N^{\text{frg}}$  are summarized in Figure 3(a) and (b) for  $\text{SrTiO}_3$  and  $\text{SrTiO}_{2.75}\text{H}_{0.25}$ , respectively. In Figure 3, the different colours denote the vacancy diffusion coefficient of the respective fragment number.

As shown in Figure 3(a), the diffusion coefficients in  $\text{SrTiO}_3$  agree well with each other. The average and standard deviations of the oxygen vacancy diffusion coefficient are shown in Table I. The differences between the respective fragmentation types are only within several nanometres/microseconds, which is less than the value of the standard deviation.

In the  $\text{SrTiO}_{2.75}\text{H}_{0.25}$  system, the hydride and oxygen ions have two different transition barriers, with activation barriers of 0.17 and 0.6 eV, respectively. The event selection of hydride and oxygen ions can be understood based on the correlation factor of the hydride ion<sup>80</sup>. One can estimate the reaction rate for each hydride or oxygen ion based on eq. 1, and the transition rates of hydride ions are about 3000 times larger than those of oxygen ions. Thus, the vacancy transition was dominated by hydride ions, and the initial large diffusion coefficient of vacancy is attributed

to the diffusion coefficient of hydride ion itself ( $D_H$ ). On the other hand, the diffusion of hydride ion in equilibrium state ( $D_H^*$ ) is highly correlated with the migration of oxygen ion as follows:

$$D_H^* = f_H D_H \quad (13)$$

$$f_H = \frac{\frac{2}{1-f} \left( \frac{r_H}{r_O} \chi_H f_H + \chi_O f_O \right)}{2 \frac{r_H}{r_O} + \frac{2}{1-f} \left( \frac{r_H}{r_O} \chi_H f_H + \chi_O f_O \right)}, \quad (14)$$

where  $f_H$  and  $f_O$  are the correlation factor for hydride and oxygen ion, and  $\chi_H$ , and  $\chi_O$  are fractional concentration of hydride and oxygen ion. The correlation factor can be estimated by first principle simulation (See ref.<sup>80,85</sup> for more detail). In the target temperature, the value of  $f_H$  is order  $10^{-3}$ . Thus, the actual hydride ion diffusion coefficients ( $D_H^*$ ) is significantly less than the diffusion coefficients of hydride ion itself ( $D_H$ ), and we observed such a decrease of diffusion coefficients of hydride ion in Figure 3(b). In comparison with conventional kMC approach, such vacancy diffusion with a mixture of different transition barriers can also be reasonably reproduced by the fragment kMC approach.

Furthermore, the temperature dependence of the vacancy diffusion coefficient was evaluated to demonstrate the accuracy of the fragment kMC method. For this purpose, the vacancy diffusion coefficients in both  $\text{SrTiO}_3$  and  $\text{SrTiO}_{2.75}\text{H}_{0.25}$  were evaluated for the temperatures 500, 550, 600, 650, and 700 K,

respectively. A comparison of the results between the conventional kMC and fragment kMC (where the number of fragments is 80) approaches is shown in Figure 4. A perfect agreement is observed between the results with and without fragmentation for both  $\text{SrTiO}_3$  and  $\text{SrTiO}_{2.75}\text{H}_{0.25}$ . The agreement between the diffusion coefficients with and without the fragmentation approach also proves that the developed fragment kMC method works for simulation of vacancy diffusion of oxygen and hydride ions.

Finally, the efficiency of the kMC approach was evaluated for vacancy diffusion in the  $\text{SrTiO}_{2.75}\text{H}_{0.25}$  system. For this purpose, the parallel efficiency of vacancy diffusion was evaluated with  $600^3$  unit cells from a single core to 216 cores (where the number of fragments ranged from 10 to 2160). The results are shown in Figure 5(a). If the number of fragments and the number of CPUs are small, the calculation requires to update the respective event information for the entire system, and then a large amount of atomic information has to be stored and accessed, operations that take additional computational time. Thus, the simulation with a small number of CPU cores was indeed inefficient. Increasing the number of CPU cores drastically reduced the computational time (Figure 5(a)). In the simulation with more than 32 cores, the computational time showed al-

most perfect parallel efficiency. The computational time with 1 CPU core is 2850 min, and the computational time is reduced to 3.1 min with 32 CPU cores, and 0.6944 min with 216 CPU cores. (140 % parallel efficiency estimated the computational time between 32 CPU and 216 CPU).

For further evaluation of the feasibility of the proposed kMC approach, the parallel efficiency with a relatively large system of  $1200^3$  unit cells was evaluated from 32 to 1800 cores (Figure 5(b)). Like with the parallel efficiency shown in Figure 5(a), the computational time could be reduced to 3.61 and 2.6 min with 512 and 1728 CPU cores, and we achieved a reduction in computational time by a factor of 24 and 33 in comparison with 32 CPU cores, and the parallel efficiency of 512 and 1728 CPU cores was 148.6 and 61.1%. Comparison of the parallel efficiency with the other simulation software is also listed in TABLE II. The parallel efficiency in this study shows reasonable performance in comparison with the other previous studies. Thus, the developed fragment kMC approach could be successfully applied to large-scale atomic diffusion by using a high-performance computing system. Note that the parallel efficiency is not main factor for determining the quality of kMC soft, and another merit of fragment kMC is the simple structure of

the method (The details will be shown in <https://github.com/hiroyanakata/kMC.v01>).

## B. Oxygen vacancy diffusion with dopant and defect interaction

It is also important to treat the interaction between vacancy and dopant in kMC model, because the diffusion coefficients strongly depend on the dopant. For this purpose, the transition rate in Eq. 1 is reformulated based on the recent review of Koettgen et. al.<sup>54</sup>:

$$k_i^I = A \exp \left[ -\frac{E_a + \Delta E^{\text{site}}/2}{RT} \right], \quad (15)$$

where the  $\Delta E^{\text{site}}$  is potential energy difference between the final and initial vacancy site, and the energy for each site  $E^{\text{site}}$  is calculated as follows:

$$E^{\text{site}} = \sum_i^{n_{\text{type}}} \sum_j^{m_{\text{neighbor}}} N_{i,j} E_{i,j}^{\text{site}}, \quad (16)$$

where  $n_{\text{type}}$  is number of different atom types (e. g. dopant-vacancy, and vacancy-vacancy interactions), and  $m_{\text{neighbor}}$  is number of nearest neighbors sites taken into account in the simulation model, and  $E_{i,j}^{\text{site}}$  is the potential energy for respective site positions, which are evaluated by first principle method.

In this section, the effectiveness of the additional interaction potential in the fragment kMC model is evaluated using Fe dopant in  $\text{SrTiO}_3$ <sup>86</sup> as for the pilot test. The potential energy is estimated

by first principle simulation using CASTEP program<sup>87,88</sup> with Perdew-Burke-Ernzerhof (PBE+U) functional.<sup>89-91</sup> The Hubbard parameter  $U$  for Ti and Fe are set to  $U = 3$  eV and  $U = 5$  eV, respectively.<sup>92</sup> The results of V-Fe interaction and V-V interaction are shown in TABLE III.

Using the obtained potential energy interactions, the fragment kMC simulation is performed, and the results of diffusion coefficient are compared between with and without the Fe dopant. The concentration of Fe and oxygen vacancies are 0.1 %, which is slightly higher concentration than actual experiment<sup>86</sup> to evaluate the dopant effect of the diffusion coefficient clearly.

The results of diffusion coefficients are shown in Figure 6. The oxygen vacancy diffusion coefficient in pure  $\text{SrTiO}_3$  is depicted in magenta open square in Figure 6. Inclusion of V-Sr interaction drastically reduced the oxygen vacancy diffusion coefficient (See blue open circle). It should be noted that the consideration of only V-Fe interaction overestimated the reduction of vacancy diffusion. Thus, additional inclusion of V-V interaction is significantly important to estimate diffusion coefficients of Fe doped  $\text{SrTiO}_3$ . The comparison between red closed square and blue open circle shows that the inclusion of V-V interaction accelerate the vacancy diffusion, which suggest the vacancy diffusion

mechanism as follows: First, each Fe atom can trap oxygen vacancy. Then the trapped oxygen vacancies act as a repulsion force to the other oxygen vacancies, which results in the acceleration of oxygen vacancy diffusion. Such interactions (V–Fe, and V–V) can be reasonably considered in the fragment kMC method.

We also investigate the effect of V–V interaction on the diffusion coefficient in pure SrTiO<sub>3</sub>. Then we do not observed much difference between with and without the V–V interaction in pure SrTiO<sub>3</sub> (green closed circle and magenta open square in Figure 6). Because the concentration of oxygen vacancy is low<sup>86</sup>, it is seldom to meet the oxygen vacancy with each other.

### C. Oxygen and hydride ions diffusion coefficients in SrTiO<sub>3</sub> and BaTiO<sub>3</sub>

Another advantage of the fragment kMC programme is the efficient evaluation of the diffusion coefficient for independent hydride or oxygen ions. Because the number of vacancies is significantly lower than the number of oxygen and hydride ions, the standard kMC approach generates an event list based on the vacancy, so the event selection process can be significantly reduced in comparison with the explicit update of oxygen or hydride ions. By contrast, the fragment kMC randomly selects

the possible event based on the atoms in the system of interest, and therefore the event selection scheme can be extended not only to vacancy diffusion, but also to the explicit diffusion of oxygen or hydride ions.

As for the pilot test of the fragment kMC approach, the oxygen and hydride ion diffusion coefficients were evaluated for both SrTiO<sub>(3-x)</sub>H<sub>x</sub> and BaTiO<sub>(3-x)</sub>H<sub>x</sub>, where the hydride ions concentrations were 0.25, 0.35, and 0.45, respectively. To evaluate the apparent activation barrier for the respective hydride and oxygen ions, the simulations were performed for 550, 600, 650, and 700 K; thus, 24 types of kMC simulations were performed to evaluate the respective activation barriers.

The results for the oxygen diffusion coefficients are shown in Figure 7(a) and (b) for SrTiO<sub>(3-x)</sub>H<sub>x</sub> and BaTiO<sub>(3-x)</sub>H<sub>x</sub>, respectively. In both cases, the oxygen diffusion is the rate determining step for vacancy diffusion, and thus the diffusion coefficients of oxygen vacancy do not vary with the concentration of hydride ions.

The diffusion coefficient of hydride ions was evaluated, and the results were compared with the diffusion coefficient of oxygen. The results for the hydride ions diffusion coefficient are shown in Figure 7(c) and (d) for SrTiO<sub>(3-x)</sub>H<sub>x</sub> and BaTiO<sub>(3-x)</sub>H<sub>x</sub>, respectively. As shown in Figure 7(c) and (d), the diffusion coefficients vary signifi-

cantly with hydride ions concentration ( $x = 0.25, 0.35, 0.45$ ).

The hydride ions diffusion is the vacancy-mediated diffusion, and this result can be understood based on the change of the correlation factor<sup>80</sup>. The correlation factor in eq. 14 changes from  $2.40 \times 10^{-3}$  to  $4.30 \times 10^{-3}$  with the increase of hydride ions concentration from 0.25 to 0.45, which suggest that the vacancy mediated hydrogen diffusion is significantly slowed down in the case of low concentration of hydrogen. The result estimated by kMC is consistent compared to the analysis of the correlation factor approach.

To evaluate the diffusion in more detail, the apparent activation barrier of hydride ions was evaluated for each hydride ions concentration ( $x = 0.25, 0.35, \text{ and } 0.45$ ). The results for the apparent activation barrier from the kMC simulation are summarized in Table IV. The activation barriers were 0.545 and 0.700 eV for  $\text{SrTiO}_{2.75}\text{H}_{0.25}$  and  $\text{BaTiO}_{0.75}\text{H}_{0.25}$ , respectively. Thus, the obtained apparent activation barriers also suggest that oxygen migration blocks the diffusion of hydride ions when the concentration of hydride ions is low ( $x = 0.25$ ). Then, the activation barriers decrease with the increase in hydride ions concentration; the apparent activation barriers for  $x = 0.45$  were 0.300 and 0.410 eV in  $\text{SrTiO}_{(3-x)}\text{H}_x$  and  $\text{BaTiO}_{(3-x)}\text{H}_x$ , respectively.

#### D. Oxygen diffusion in $\mu$ -scale $\text{BaTiO}_3$ model

To demonstrate the effectiveness of the fragment kMC approach, the  $\mu$ -scale  $\text{BaTiO}_3$  model is constructed, and the oxygen vacancy diffusion is evaluated. The  $\text{BaTiO}_3$  is a material that is important for industry, and the oxygen vacancy diffusion under voltage application has a crucial role in insulation deterioration. Thus, the oxygen vacancy diffusion in  $\text{BaTiO}_3$  was investigated to demonstrate the effectiveness of the fragment kMC approach.

Likewise with the other ceramic materials, we practically use the polycrystalline  $\text{BaTiO}_3$  for MLCC, whose grain boundary structures have not yet been understood in detail. In the simulation perspective, it is also difficult to make such a complex grain boundary structures at current stage of the fragment kMC approach. As for the initial pilot test whether the  $\mu$ -scale oxygen vacancy diffusion can be evaluated or not, the simulation models are separated into respective grains, and we introduce an artificial intermediate  $\text{BaTiO}_3$  layer to separate the respective grains, and the transition of oxygen vacancies inside the grain are investigated. The details of the test model are described as follows.

The Voronoi tessellation method<sup>93</sup> was used to make the geometry of  $\text{BaTiO}_3$  test model, and the simulation model of this

study are shown in Figure 8(a). The test model is constructed in two dimensions (Figure 8) for simplicity, but the actual kMC simulation was performed in three dimensions. The white colour denotes the grain, the black solid line is the grain boundary, and the orange circle is the edge of the grain boundary. The test model was constructed to satisfy the periodic boundary condition (PBC), and the centre region depicted with an open rectangular (blue dotted line) was explicitly treated by kMC, where the size of the simulation model was  $641.6 \text{ nm} \times 160.4 \text{ nm} \times 962.4 \text{ nm}$  and the model contained 7,680,000,000 atoms in the system.

In this study, the activation barrier over the respective boundary region was set higher than those in the bulk area, by adding positive electrostatic potential (0.2 eV). The value 0.2 eV was determined from the reported experimental study for oxygen vacancy diffusion<sup>94</sup>, and thus, the total activation barrier through the boundary was set to 0.9 eV. As noted, the additional intermediate layers are set nearby the grain boundaries to remove the effect of vacancy transition over the grains as shown in Figure 8(b). The analysis concentrated on the oxygen vacancy diffusion within the respective grains, and we define the region between the grains and the additional intermediate layer as the layer boundary region.

In this study, the electrostatic potential was considered by solving the Poisson equation<sup>95</sup>. To apply the bias voltage, the boundary conditions were set to 10.0 eV for the top of the  $z$ -axis and  $-10.0 \text{ eV}$  for the bottom of the  $z$ -axis, and the PBC was applied for the  $x$ - and  $y$ -axes to solve the Poisson equation. The electrostatic potential after applying the bias voltage is shown in Figure 8(c). Because we applied the bias voltage along the  $z$ -axis, the PBC of the  $z$ -axis is broken. Instead of the PBC, the open boundary approximation was applied. If the oxygen vacancy diffuses over the boundary, we consider that the same amount of oxygen vacancies enters from the other side of the boundary region. This approximation maintains the total number of oxygen vacancies.

The distribution of oxygen vacancies obtained by a 5 ms simulation is shown in Figure 9. It can be observed that the oxygen vacancies tend to gather around the bottom of the layer boundary (The charge of vacancy is compensated by the reduction of Titanium from IV to III). The highest oxygen vacancy concentration can be found around  $x = 138$  and  $z = 686$ , and the density of oxygen vacancy in the highest region is  $1.4 \text{ nm}^{-3}$ . The average vacancy concentration in this study was  $0.0465 \text{ nm}^{-3}$ , and an oxygen vacancy concentration about 30 times larger was observed. It should be noted that we have also

found some oxygen vacancy concentration in the bottom of intermediate layers (nearby the top of grain), because of the artificial separation of respective grains. More detail information for the oxygen vacancy concentration in the intermediate layers are shown in supplementary materials, and here we focus on the oxygen vacancy concentration inside the grain.

The highest oxygen vacancy concentration can be found near the triangular layer boundary on the bottom of Figure 9(a), and the detailed distribution of oxygen vacancies is shown in Figure 10(a). As shown in Figure 10(a), the oxygen vacancies diffuse to increasingly low regions, but the layer boundary area prohibits to transfer the vacancy further, and the vacancy migrates to the next lower layer boundary area. As a result, the oxygen vacancies gather to the lowest edge area (See Figure 10(a)).

The grain size is also an important factor to determine the oxygen vacancy density in the edge area. Figure 10(b) and Figure 9(b) show the oxygen vacancy density at the edge area in the case of small grain size. The total number of oxygen vacancies in small grains is lower than in large grains, which also results in a smaller vacancy concentration in the edge area. Compared with the results in Figure 10(a), the edge in a small grain (Figure 10(b)) has a lower oxygen vacancy con-

centration, and the concentration of oxygen vacancies is about 35.7% lower than the highest oxygen vacancy concentration.

Another type of oxygen vacancy concentration can be found in the region where the layer boundary is a horizontal line (parallel to the  $x$ -axis, see Figure 9(c)). The distribution of oxygen vacancies around the horizontal layer boundary is shown in Figure 10(c), where it can be observed that the number of oxygen vacancies is lower than that of the edge area, even for the largest grain size (Figure 9(c)).

In summary, the simulation results indicate that the oxygen vacancy diffusion processes occur as follows. The oxygen vacancies tend to be trapped in the layer boundary area, and going through the boundary region, the vacancies are finally trapped at the edge area. Thus, without the edge area (i.e., the layer boundary is parallel to the  $x$ -axis), the oxygen vacancy concentration is very low. The oxygen vacancy migration inside the respective grains is considered to be reasonable based on the general behaviour of oxygen vacancy migration in grains<sup>14,15,19</sup>, and the above pilot test suggest that the developed fragment kMC can simulate the oxygen migration in such a large  $\mu$  scale BaTiO<sub>3</sub> model with a fully atomistic computational model.

## V. CONCLUSION

In this study, the fragment kMC method is proposed. This approach introduces the auxiliary value  $R^{\max}$ , and the event selection can be decomposed into atomic-based fragments. The kMC method can be easily parallelized towards calculation of atomic migrations. The diffusion coefficients perfectly agree with the conventional kMC simulation, and the parallel efficiency of fragment kMC was good enough until the number of CPU cores reached 1728.

The method can be straightforwardly extended to analyse the diffusion coefficient for independent atomic types. The respective hydride ions and oxygen diffusion coefficients were evaluated in perovskite  $\text{SrTiO}_{(3-x)}\text{H}_x$  and  $\text{BaTiO}_{(3-x)}\text{H}_x$  systems. The simulation was performed with various hydride ions compositions ( $x = 0.25, 0.35, 0.45$ ), which were slightly difficult to predict using conventional kMC. Then, the simulation provided good prediction of the diffusion coefficient of hydride ions at reasonable computational cost.

Finally, the fragment kMC was extended to simulate the  $\mu$  scale  $\text{BaTiO}_3$  under bias voltage application. We found that the oxygen vacancy concentration in the edge region was the highest, and the obtained results were reasonable based on the general be-

haviour of oxygen migration in  $\text{BaTiO}_3$  materials. Thus, we conclude that the developed fragment kMC programme can be useful for simulating many kinds of atomistic diffusion in crystal systems, and we hope that the proposed method can be widely used to understand the diffusion mechanism in the field of materials and chemistry.

## ACKNOWLEDGMENT

We thank R.I.I.T. at Kyushu University (Japan) for providing computational resources. This research also used computational resources of the Fujitsu PRIMERGY CX400M1/CX2550M5(Oakbridge-CX) by Information Technology Center, The University of Tokyo through the HPCI System Research project (Project ID:hp200015).

## REFERENCES

- <sup>1</sup>J. Cerdà, J. Arbiol, G. Dezanneau, R. Diaz, and J. Morante, *Sensors and Actuators B: chemical* **84**, 21 (2002).
- <sup>2</sup>W. Menesklou, H.-J. Schreiner, K. H. Härdtl, and E. Ivers-Tiffée, *Sensors and Actuators B: Chemical* **59**, 184 (1999).
- <sup>3</sup>B. Nagaraj et al., *Applied physics letters* **74**, 3194 (1999).
- <sup>4</sup>E. J. Yoo, M. Lyu, J.-H. Yun, C. J. Kang, Y. J. Choi, and L. Wang, *Advanced Mate-*

- rials **27**, 6170 (2015).
- <sup>5</sup>K. Szot, W. Speier, G. Bihlmayer, and R. Waser, *Nature materials* **5**, 312 (2006).
- <sup>6</sup>Y. Zhao, L. Xu, L. Mai, C. Han, Q. An, X. Xu, X. Liu, and Q. Zhang, *Proceedings of the National Academy of Sciences* **109**, 19569 (2012).
- <sup>7</sup>J. Suntivich, H. A. Gasteiger, N. Yabuuchi, H. Nakanishi, J. B. Goodenough, and Y. Shao-Horn, *Nature chemistry* **3**, 546 (2011).
- <sup>8</sup>H. Kishi, Y. Mizuno, and H. Chazono, *Japanese journal of applied physics* **42**, 1 (2003).
- <sup>9</sup>W. Cao and C. A. Randall, *Journal of Physics and Chemistry of Solids* **57**, 1499 (1996).
- <sup>10</sup>C. A. Randall, N. Kim, J.-P. Kucera, W. Cao, and T. R. ShROUT, *Journal of the American Ceramic Society* **81**, 677 (1998).
- <sup>11</sup>K.-I. Park et al., *Advanced materials* **26**, 2514 (2014).
- <sup>12</sup>T. Ishihara, *Perovskite oxide for solid oxide fuel cells*, Springer Science & Business Media, 2009.
- <sup>13</sup>C.-K. Yang, Y. Yamazaki, A. Aydin, and S. M. Haile, *Journal of Materials Chemistry A* **2**, 13612 (2014).
- <sup>14</sup>G. Yang, G. Lian, E. Dickey, C. A. Randall, D. Barber, P. Pinceloup, M. Henderson, R. Hill, J. Beeson, and D. Skamser, *Journal of applied physics* **96**, 7500 (2004).
- <sup>15</sup>H. Chazono and H. Kishi, *Japanese Journal of Applied Physics* **40**, 5624 (2001).
- <sup>16</sup>H. Chazono and H. Kishi, Effect of ho amount on microstructure and electrical properties of ni-mlcc, in *Key engineering materials*, volume 248, pages 183–186, Trans Tech Publ, 2003.
- <sup>17</sup>D. F. Hennings, *Journal of the european ceramic society* **21**, 1637 (2001).
- <sup>18</sup>K. Albertsen, D. Hennings, and O. Steigelmann, *Journal of Electroceramics* **2**, 193 (1998).
- <sup>19</sup>D. B. Strukov, F. Alibart, and R. S. Williams, *Applied Physics A* **107**, 509 (2012).
- <sup>20</sup>G. Yang, E. Dickey, C. A. Randall, M. Randall, and L. Mann, *Journal of applied physics* **94**, 5990 (2003).
- <sup>21</sup>R. M. Waser, *Journal of the American Ceramic Society* **72**, 2234 (1989).
- <sup>22</sup>S. Shirasaki, H. Yamamura, H. Haneda, K. Kakegawa, and J. Moori, *The Journal of Chemical Physics* **73**, 4640 (1980).
- <sup>23</sup>J.-i. Itoh, D.-C. Park, N. Ohashi, I. Sakaguchi, I. Yashima, H. Haneda, and J. Tanaka, *Journal of the Japan Society of Powder and Powder Metallurgy* **49**, 626 (2002).
- <sup>24</sup>J.-i. ITOH, D.-C. PARK, N. OHASHI, I. SAKAGUCHI, I. YASHIMA, H. HANEDA, and J. TANAKA, *Journal of the Ceramic Society of Japan* **110**, 495

- (2002).
- <sup>25</sup>A. Hasegawa, S. Fujitsu, K. Koumoto, and H. Yanagida, *Japanese journal of applied physics* **30**, 1252 (1991).
- <sup>26</sup>T. Frömling, J. Hou, W. Preis, W. Sitte, H. Hutter, and J. Fleig, *Journal of Applied Physics* **110**, 043531 (2011).
- <sup>27</sup>M. Kessel, R. De Souza, H.-I. Yoo, and M. Martin, *Applied Physics Letters* **97**, 021910 (2010).
- <sup>28</sup>R. De Souza, *Advanced Functional Materials* **25**, 6326 (2015).
- <sup>29</sup>G. Lewis and C. Catlow, *Journal of Physics C: Solid State Physics* **18**, 1149 (1985).
- <sup>30</sup>B. P. Uberuaga and L. J. Vernon, *Solid State Ionics* **253**, 18 (2013).
- <sup>31</sup>P. Erhart, A. Klein, R. G. Egdell, and K. Albe, *Physical review B* **75**, 153205 (2007).
- <sup>32</sup>W. Münch, G. Seifert, K. Kreuer, Maier, and J, *Solid State Ionics* **97**, 39 (1997).
- <sup>33</sup>L. Zhang, B. Liu, H. Zhuang, P. R. Kent, V. R. Cooper, P. Ganesh, and H. Xu, *Computational Materials Science* **118**, 309 (2016).
- <sup>34</sup>L. Zhang, B. Liu, H. Zhuang, P. R. Kent, V. R. Cooper, P. Ganesh, and H. Xu, *Computational Materials Science* **118**, 309 (2016).
- <sup>35</sup>C. Shi, M. Yoshino, and M. Morinaga, *Solid State Ionics* **176**, 1091 (2005).
- <sup>36</sup>M. E. Björketun, P. G. Sundell, and G. Wahnström, *Physical Review B* **76**, 054307 (2007).
- <sup>37</sup>K.-D. Kreuer, *Annual Review of Materials Research* **33**, 333 (2003).
- <sup>38</sup>K. Kreuer, *Solid State Ionics* **125**, 285 (1999).
- <sup>39</sup>S. G. Kang and D. S. Sholl, *RSC Advances* **3**, 3333 (2013).
- <sup>40</sup>H. Zhang, A. H. Ramadan, and R. A. De Souza, *Journal of Materials Chemistry A* **6**, 9116 (2018).
- <sup>41</sup>H. Zhang and R. A. De Souza, *Journal of Materials Chemistry A* **7**, 25274 (2019).
- <sup>42</sup>C. Tealdi, P. Mustarelli, and M. S. Islam, *Advanced Functional Materials* **20**, 3874 (2010).
- <sup>43</sup>M. SaifuláIslam et al., *Chemical Communications* , 715 (2008).
- <sup>44</sup>D. Parfitt, A. Chroneos, A. Tarancón, and J. A. Kilner, *Journal of Materials Chemistry* **21**, 2183 (2011).
- <sup>45</sup>S. P. Waldow and R. A. De Souza, *ACS applied materials & interfaces* **8**, 12246 (2016).
- <sup>46</sup>D. Marrocchelli, L. Sun, and B. Yildiz, *Journal of the American Chemical Society* **137**, 4735 (2015).
- <sup>47</sup>C. Caron, editor, *An Introduction to Kinetic Monte Carlo Simulations of Surface Reactions*, Springer, Heidelberg in Germany, 2012.

- <sup>48</sup>G. Murch, *American Journal of Physics* **47**, 78 (1979).
- <sup>49</sup>K. E. Sickafus, E. A. Kotomin, and B. P. Uberuaga, *Radiation effects in solids*, volume 235, Springer Science & Business Media, 2007.
- <sup>50</sup>K. C. Lau, C. H. Turner, and B. I. Dunlap, *Chemical Physics Letters* **471**, 326 (2009).
- <sup>51</sup>K. C. Lau, C. H. Turner, and B. I. Dunlap, *Solid State Ionics* **179**, 1912 (2008).
- <sup>52</sup>T. Tada and N. Watanabe, *ECS Transactions* **57**, 2437 (2013).
- <sup>53</sup>S. Grieshammer, S. Eisele, and J. Koettgen, *The Journal of Physical Chemistry C* **122**, 18809 (2018).
- <sup>54</sup>J. Koettgen, S. Grieshammer, P. Hein, B. O. Grope, M. Nakayama, and M. Martin, *Physical Chemistry Chemical Physics* **20**, 14291 (2018).
- <sup>55</sup>S. Piccinin and M. Stamatakis, *ACS Catalysis* **4**, 2143 (2014).
- <sup>56</sup>C. Wu, D. Schmidt, C. Wolverton, and W. Schneider, *Journal of Catalysis* **286**, 88 (2012).
- <sup>57</sup>M. Stamatakis, Y. Chen, and D. G. Vlachos, *The Journal of Physical Chemistry C* **115**, 24750 (2011).
- <sup>58</sup>L. Yang, A. Karim, and J. T. Muckerman, *The Journal of Physical Chemistry C* **117**, 3414 (2013).
- <sup>59</sup>W. Guo, M. Stamatakis, and D. G. Vlachos, *ACS Catalysis* **3**, 2248 (2013).
- <sup>60</sup>W. Guo and D. G. Vlachos, *Nature communications* **6**, 8619 (2015).
- <sup>61</sup>S. Lin, J. Ma, L. Zhou, C. Huang, D. Xie, and H. Guo, *The Journal of Physical Chemistry C* **117**, 451 (2013).
- <sup>62</sup>S. M. Auerbach, *International reviews in physical chemistry* **19**, 155 (2000).
- <sup>63</sup>S. Matera, H. Meskine, and K. Reuter, *The Journal of chemical physics* **134**, 064713 (2011).
- <sup>64</sup>B. Temel, H. Meskine, K. Reuter, M. Scheffler, and H. Metiu, *The Journal of chemical physics* **126**, 204711 (2007).
- <sup>65</sup>M. Rieger, J. Rogal, and K. Reuter, *Physical review letters* **100**, 016105 (2008).
- <sup>66</sup>R. Pornprasertsuk, T. Holme, and F. B. Prinz, *Journal of The Electrochemical Society* **156**, B1406 (2009).
- <sup>67</sup>R. Pornprasertsuk, J. Cheng, H. Huang, and F. B. Prinz, *Solid State Ionics* **178**, 195 (2007).
- <sup>68</sup>E. W. Hansen and M. Neurock, *Chemical engineering science* **54**, 3411 (1999).
- <sup>69</sup>E. W. Hansen and M. Neurock, *Surface science* **464**, 91 (2000).
- <sup>70</sup>E. W. Hansen and M. Neurock, *Journal of Catalysis* **196**, 241 (2000).
- <sup>71</sup>K. Reuter and M. Scheffler, *Physical Review B* **73**, 045433 (2006).
- <sup>72</sup>M. Stamatakis, Y. Chen, and D. G. Vlachos, *The Journal of Physical Chemistry C* **115**, 24750 (2011).

- <sup>73</sup>J. A. Boscoboinik, C. Plaisance, M. Neurock, and W. T. Tysoe, *Physical Review B* **77**, 045422 (2008).
- <sup>74</sup>L. Kunz, F. M. Kuhn, and O. Deutschmann, *The Journal of chemical physics* **143**, 044108 (2015).
- <sup>75</sup>D.-J. Liu and J. W. Evans, *Progress in Surface Science* **88**, 393 (2013).
- <sup>76</sup>M. Stamatakis and S. Piccinin, *ACS Catalysis* **6**, 2105 (2016).
- <sup>77</sup>G. Gilmer, *Science* **208**, 355 (1980).
- <sup>78</sup>T. P. Schulze, *Journal of crystal growth* **263**, 605 (2004).
- <sup>79</sup>K. Li, H. Shang, Y. Zhang, S. Li, B. Wu, D. Wang, L. Zhang, F. Li, D. Chen, and Z. Wei, *Openkmc: a kmc design for hundred-billion-atom simulation using millions of cores on sunway taihulight*, in *Proceedings of the International Conference for High Performance Computing, Networking, Storage and Analysis*, pages 1–16, 2019.
- <sup>80</sup>X. Liu, T. S. Bjørheim, L. Vines, Ø. S. Fjellvåg, C. Granerød, Ø. Prytz, T. Yamamoto, H. Kageyama, T. Norby, and R. Haugrud, *Journal of the American Chemical Society* **141**, 4653 (2019).
- <sup>81</sup>S. Grieshammer, B. O. Grope, J. Koettgen, and M. Martin, *Physical Chemistry Chemical Physics* **16**, 9974 (2014).
- <sup>82</sup>R. A. De Souza, V. Metlenko, D. Park, and T. E. Weirich, *Physical Review B* **85**, 174109 (2012).
- <sup>83</sup>M. Kessel, R. A. De Souza, and M. Martin, *Physical Chemistry Chemical Physics* **17**, 12587 (2015).
- <sup>84</sup>X. Liu, T. S. Bjørheim, and R. Haugrud, *Journal of Materials Chemistry A* **5**, 1050 (2017).
- <sup>85</sup>J.-M. Philibert, *Atom movements-Diffusion and mass transport in solids*, EDP Sciences, 2012.
- <sup>86</sup>D. Ascienzo, O. Kurt, S. Greenbaum, T. J. Bayer, M. Russell, J. Wang, C. A. Randall, and Y. Ren, *Journal of the American Ceramic Society* **102**, 4353 (2019).
- <sup>87</sup>M. C. Payne, M. P. Teter, D. C. Allan, T. A. Arias, and J. D. Joannopoulos, *Rev. Mod. Phys.* **64**, 1045 (1992).
- <sup>88</sup>M. V., W. B., W. J. A., P. C. J., P. M. C., A. E. V., and N. R. H., *International Journal of Quantum Chemistry* **77**, 895.
- <sup>89</sup>J. P. Perdew, J. A. Chevary, S. H. Vosko, K. A. Jackson, M. R. Pederson, D. J. Singh, and C. Fiolhais, *Physical review B* **46**, 6671 (1992).
- <sup>90</sup>J. P. Perdew, K. Burke, and M. Ernzerhof, *Physical review letters* **77**, 3865 (1996).
- <sup>91</sup>V. I. Anisimov, J. Zaanen, and O. K. Andersen, *Physical Review B* **44**, 943 (1991).
- <sup>92</sup>N. Kim, N. H. Perry, and E. Ertekin, *Chemistry of Materials* **31**, 233 (2018).
- <sup>93</sup>F. Aurenhammer and R. Klein, *Handbook of computational geometry* **5**, 201 (2000).

- <sup>94</sup>C.-Y. S. Chang, I. Lubomirsky, and S. Kim, Physical Chemistry Chemical Physics **20**, 19250 (2018).
- <sup>95</sup>Y. Cao, J. Shen, C. Randall, and L.-Q. Chen, Journal of the American Ceramic Society **97**, 3568 (2014).
- <sup>96</sup>E. Vincent, C. Becquart, and C. Domain, Journal of nuclear materials **351**, 88 (2006).
- <sup>97</sup>J. Li, P. Wei, S. Yang, J. Wu, P. Liu, and X. He, Tsinghua Science and Technology **23**, 501 (2018).
- <sup>98</sup>E. Martínez, P. R. Monasterio, and J. Mariani, Journal of Computational Physics **230**, 1359 (2011).

TABLE captions.

TABLE I. Average and standard deviation (SD) of the oxygen vacancy diffusion coefficient ( $\text{\AA}\mu\text{s}$ ) in  $\text{SrTiO}_3$  single crystal.

number of fragment	Average (SD)	
1	6433	56
8	6428	75
32	6433	54
64	6385	59
125	6412	49
216	6391	66

TABLE II. Parallele efficiency comparison with previous studies.

Software	CPU cores	efficiency
LAKIMOCA <sup>96</sup>	Only Serial	N. A.
mesokMC <sup>52</sup>	32	55
Crystal-KMC <sup>97</sup>	800	56
spKMC <sup>98</sup>	256	82
this study	512	148

TABLE III. The potential energy between Vacancy and Fe (left column), and potential energy between Vacancy and Vacancy (right column) estimated by first principle simulation.

site	Dis	V-Fe	Dis	V-V
1st	1.952	0.000	2.76	0.343
2nd	4.390	0.510	3.91	0.235
3rd	5.920	0.687	4.78	0.200
4th	7.030	0.709	5.52	0.180
5th	N.A.	N.A.	6.17	0.023
6th	N.A.	N.A.	7.81	0.000

TABLE IV. Apparent activation barrier (eV) estimated by the diffusion coefficient of hydride ions. The simulation results are shown in Figure 7.

H concentration	SrTiO <sub>3</sub>	BaTiO <sub>3</sub>
0.45	0.300	0.410
0.35	0.464	0.611
0.25	0.545	0.700

### FIGURE CAPTIONS

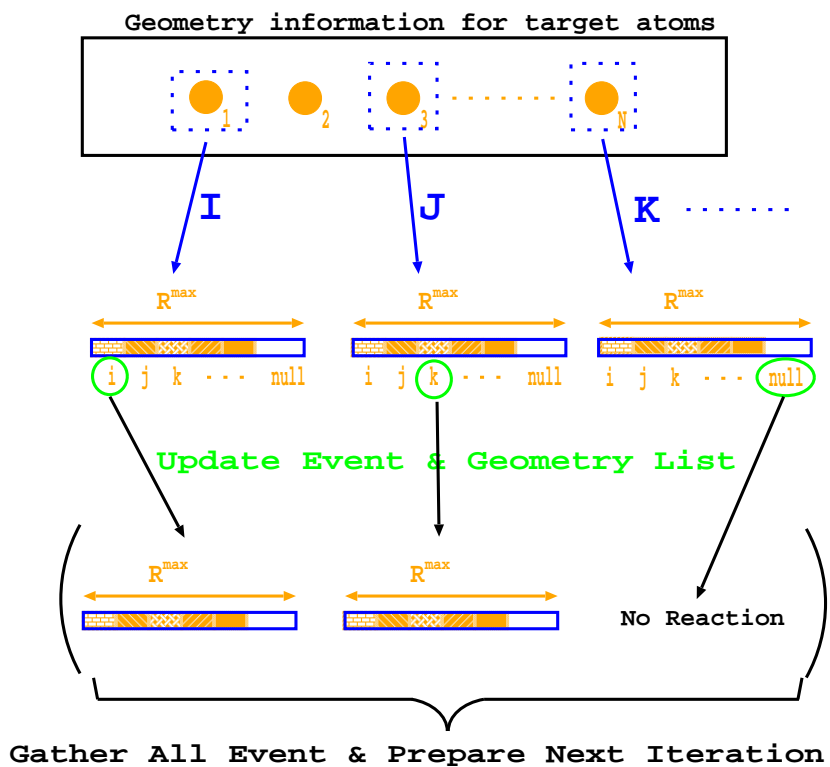


FIG. 1. Schematic illustration of how the fragment kMC method updates the event selection and the geometry update process.

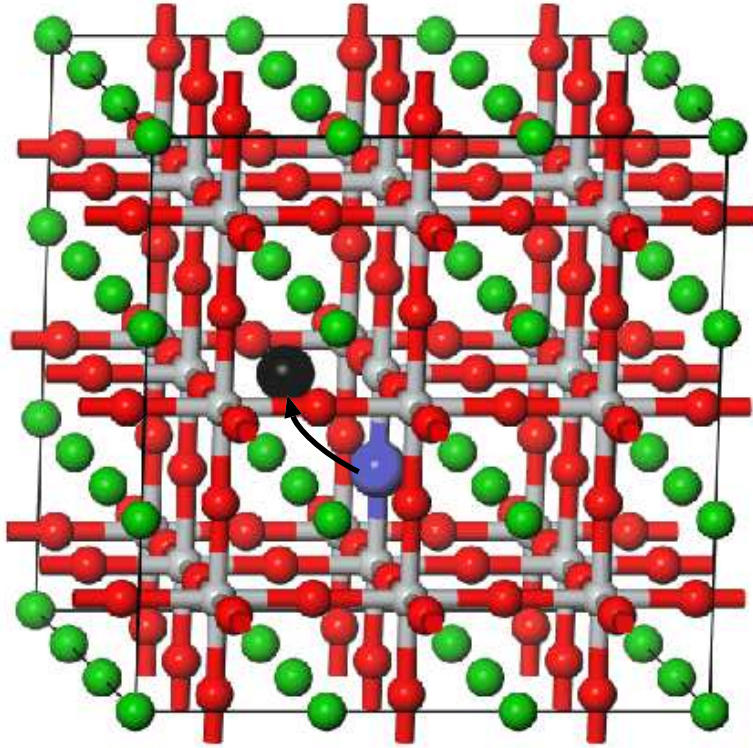


FIG. 2. Crystal structure of the  $\text{Ba}(\text{Sr})\text{TiO}_3$  system used in this study. Green, red, and gray denote the  $\text{Ba}(\text{Sr})$ ,  $\text{O}$ , and  $\text{Ti}$ , respectively. The black denote the oxygen vacancy, and the blue oxygen migrate to the black vacancy site during the kMC simulation.

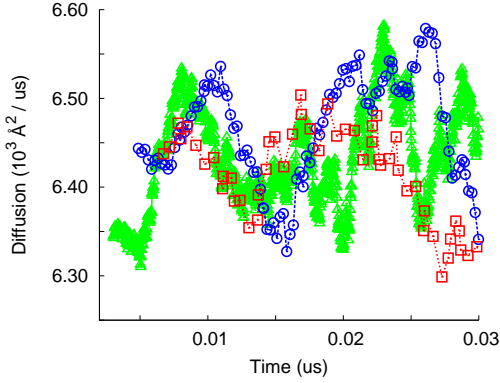
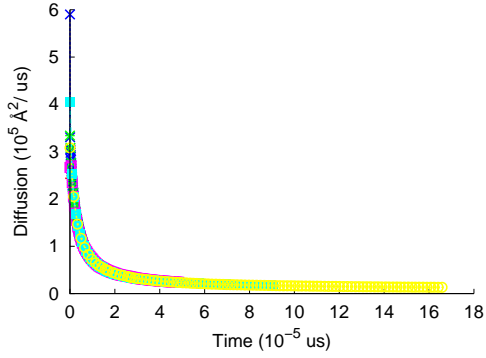
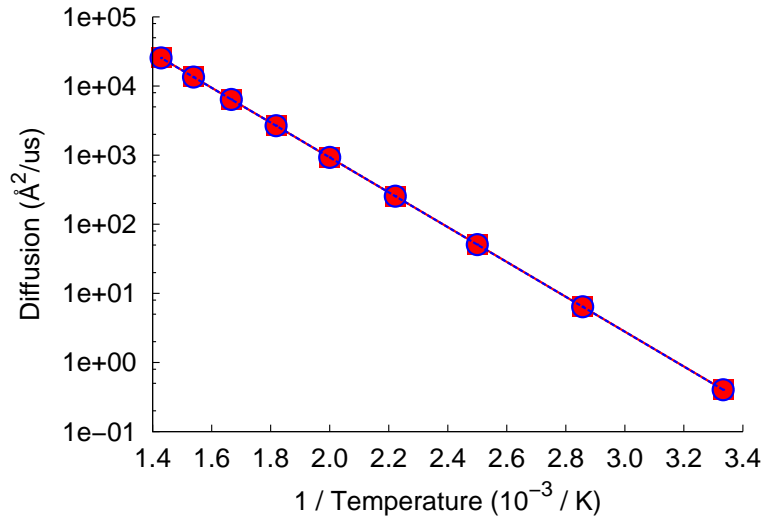
**(a)****(b)**

FIG. 3. Comparison between the vacancy diffusion coefficients obtained with different numbers of fragments. The unit of the vacancy diffusion coefficient is  $\text{\AA}^2/\text{us}$ . (a)  $\text{SrTiO}_3$ : The red, blue, and green lines denote the results with 216 and 80 fragments and conventional kMC, respectively. (b)  $\text{SrTiO}_{(3-x)}\text{H}_x$  with  $x = 0.25$ : Red, blue, green, magenta, sky blue, and yellow denote the results with conventional kMC and 1, 8, 32, 64, 125, and 216 fragments, respectively.

(a)



(b)

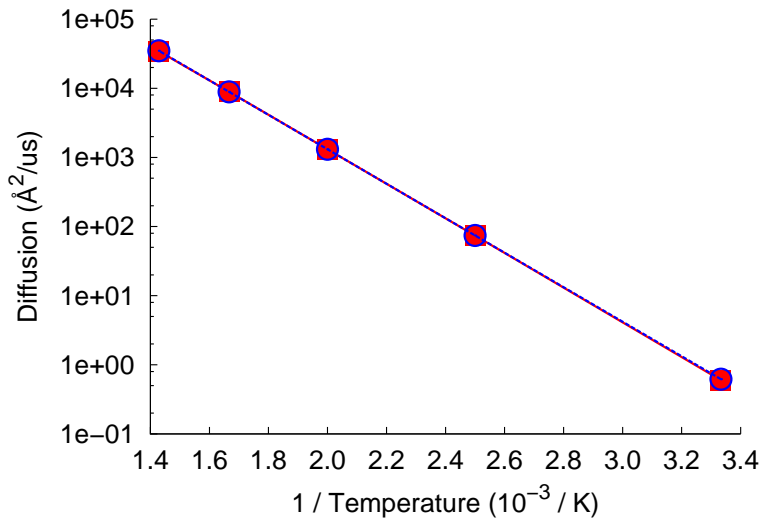
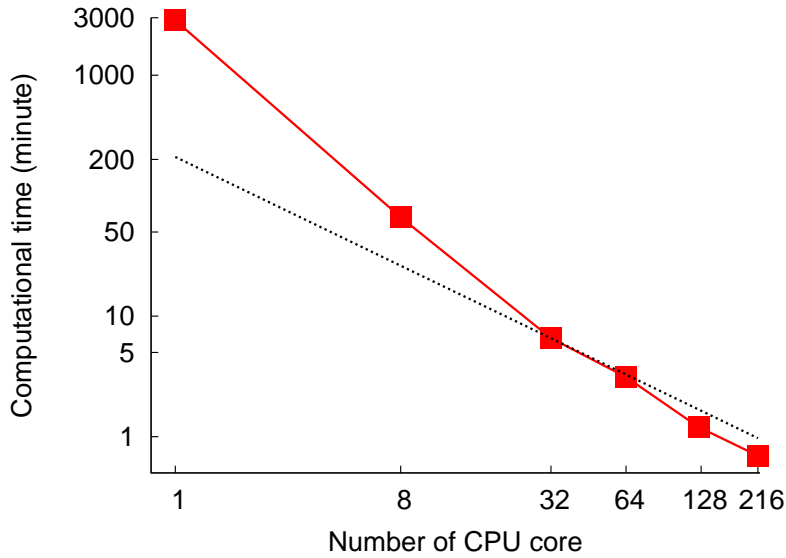


FIG. 4. The average vacancy diffusion coefficient for different temperatures. Comparison between (blue) standard kMC and (red) fragment kMC for (a)  $\text{SrTiO}_3$  and (b)  $\text{SrTiO}_{(3-x)}\text{H}_x$  with  $x = 0.25$ . The number of fragments is 80.

**(a)**



**(b)**

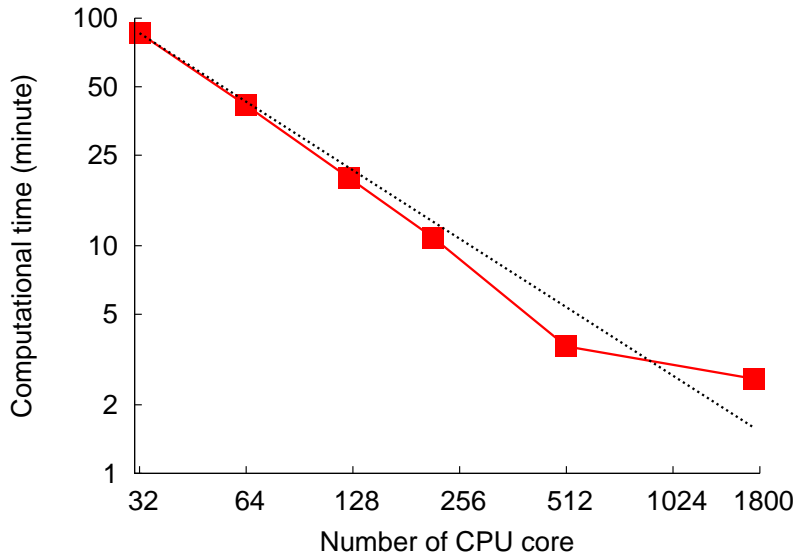


FIG. 5. Computational timing and its parallel efficiency of fragment kMC. The black dashed line is the ideal computational time estimated by using the computational time with 32 cores. (a) for  $600 \times 600 \times 600$  unit cells from 1 to 216 cores and (b) for  $1200 \times 1200 \times 1200$  unit cells from 32 to 1728 cores.

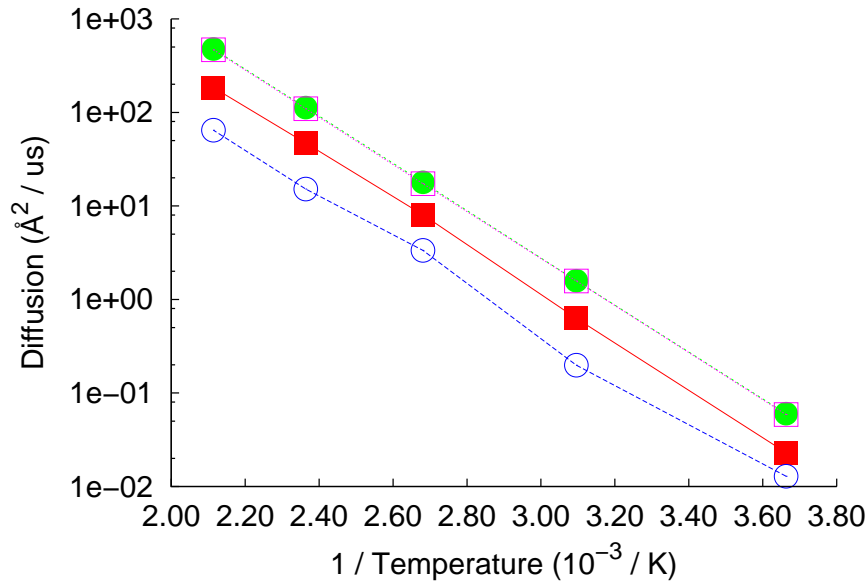


FIG. 6. Diffusion coefficient for doped SrTiO<sub>3</sub>. Red closed square is diffusion coefficients of Fe doped SrTiO<sub>3</sub> with Sr-V and V-V interaction, and blue open circle is those with Sr-V interaction only. Green closed circle is the diffusion coefficients of pure SrTiO<sub>3</sub> with V-V interaction, and magenta open square is those with no interaction.

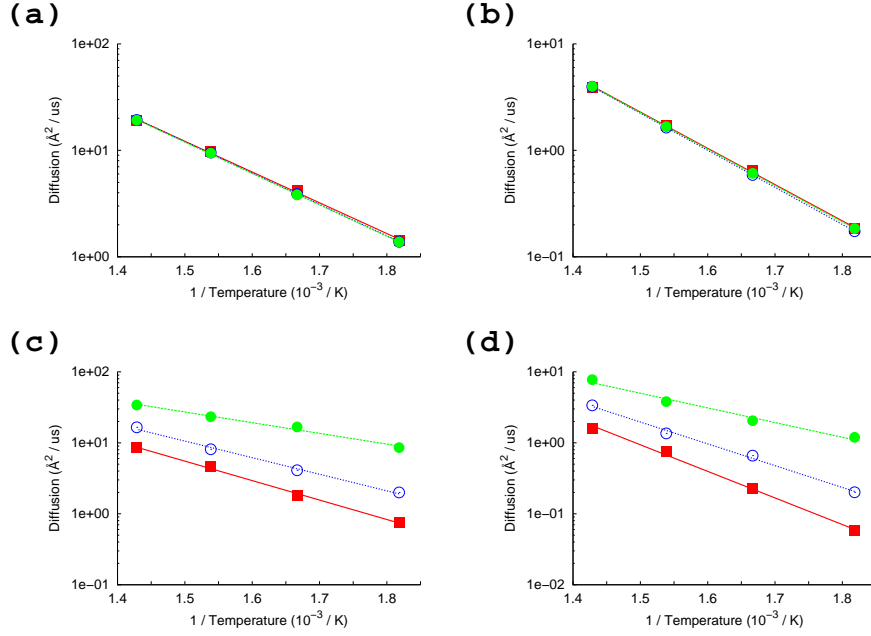


FIG. 7. Oxygen and hydride ions diffusion coefficients from 550 to 700 K for (a) and (c)  $\text{SrTiO}_{(3-x)}\text{H}_x$  and for (b) and (d)  $\text{BaTiO}_{(3-x)}\text{H}_x$ . Red closed squares, blue open circles, and green closed circles illustrate the simulation results for  $x = 0.25$ ,  $0.35$ , and  $0.45$ , respectively. The oxygen vacancy diffusion coefficients are shown in (a), and (b), while the hydrogen diffusion coefficients are shown in (c), and (d).

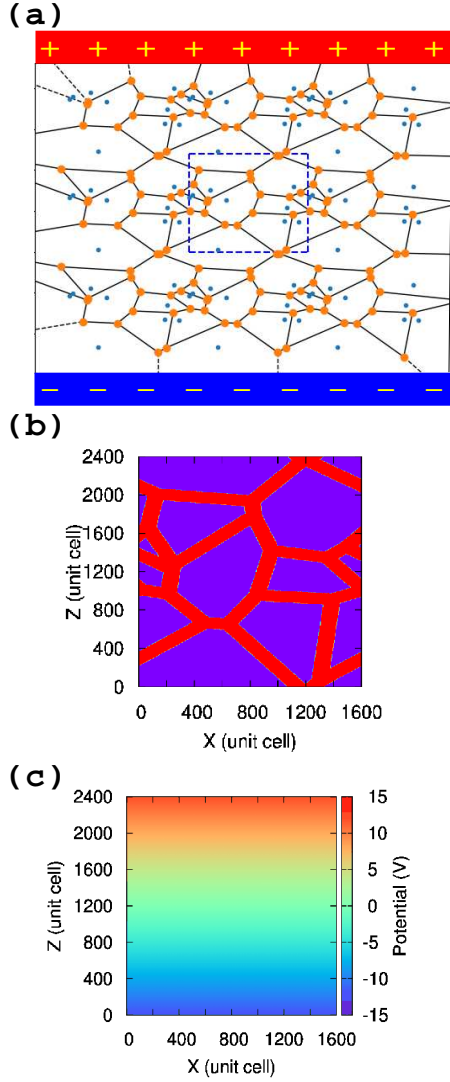


FIG. 8. Simulation model for polycrystalline  $\text{BaTiO}_3$ . (a) Overview of the periodic simulation model used in this study, where the blue dotted line denotes the actual simulated area. (b) Detailed simulation model for oxygen diffusion analysis, where the purple colour denotes the respective grain, and the oxygen vacancy concentration is evaluated for each grain area. The red colour denotes the intermediate layer between the grains. (c) Schematic illustration of applying bias voltage and electrostatic potential.

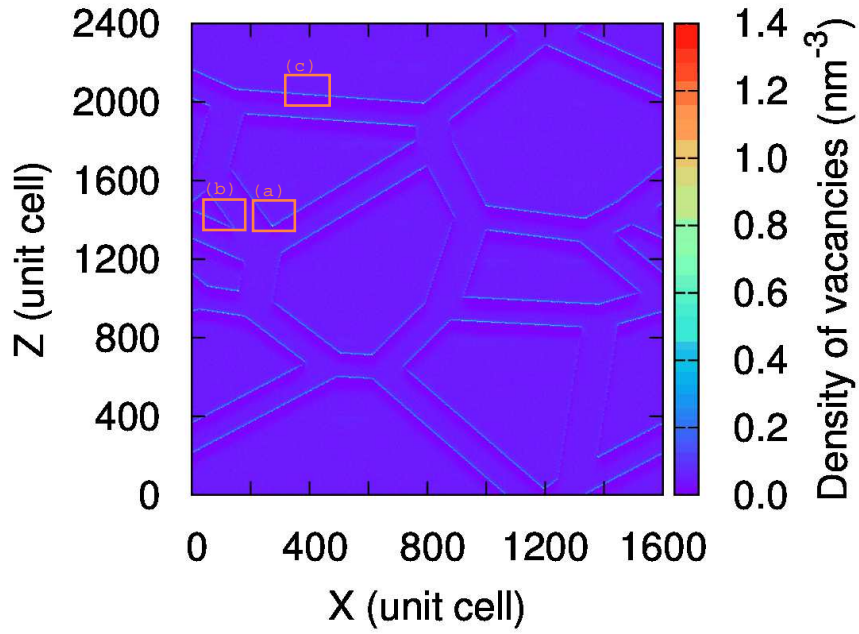


FIG. 9. The oxygen vacancy concentration of the simulation model in Figure 8(b). Detailed analysis was performed for the orange open square areas (a), (b), and (c). See the main text and Figure 10 for detail.

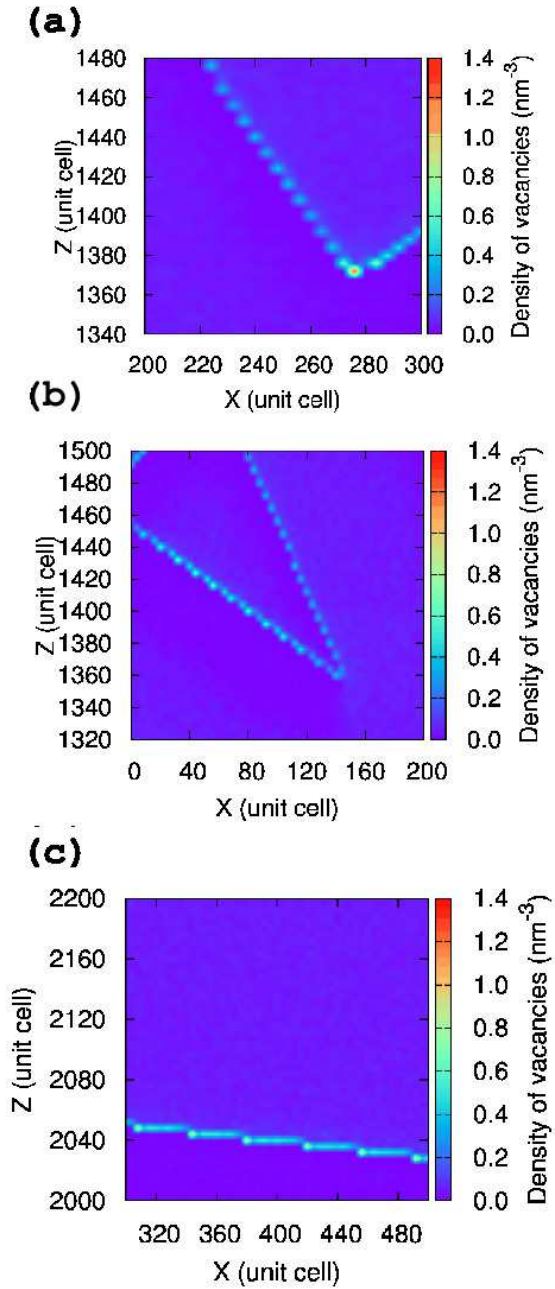


FIG. 10. Oxygen vacancy concentration of the respective areas shown in Figure 9(a), (b), and (c).